



HAL
open science

Fracture parameter identification by Digital Image Correlation and Finite Fracture Mechanics for millimeter-scale samples

Thomas Duminy, Aurélien Doitrand, Sylvain Meille

► **To cite this version:**

Thomas Duminy, Aurélien Doitrand, Sylvain Meille. Fracture parameter identification by Digital Image Correlation and Finite Fracture Mechanics for millimeter-scale samples. *Engineering Fracture Mechanics*, 2024, 295, pp.109770. 10.1016/j.engfracmech.2023.109770 . hal-04316450

HAL Id: hal-04316450

<https://hal.science/hal-04316450>

Submitted on 30 Nov 2023

HAL is a multi-disciplinary open access archive for the deposit and dissemination of scientific research documents, whether they are published or not. The documents may come from teaching and research institutions in France or abroad, or from public or private research centers.

L'archive ouverte pluridisciplinaire **HAL**, est destinée au dépôt et à la diffusion de documents scientifiques de niveau recherche, publiés ou non, émanant des établissements d'enseignement et de recherche français ou étrangers, des laboratoires publics ou privés.

Fracture parameter identification by Digital Image Correlation and Finite Fracture Mechanics for millimeter-scale samples

Thomas Duminy^{✉a}, Aurélien Doitrand^a, Sylvain Meille^a

^aUniv Lyon, INSA Lyon, UCBL, MATEIS UMR CNRS 5510, Villeurbanne, F-69621, France
e-mail: thomas.duminy@insa-lyon.fr
postal address: 7 Avenue Jean Capelle, 69100 Villeurbanne, FRANCE

Abstract

In situ wedge splitting tests are conducted on millimeter-size PMMA samples. A method to determine the material tensile strength and critical energy release rate (ERR) from digital image correlation (DIC) and a full finite element implementation of the coupled criterion (CC) is proposed. The best material parameter identification is achieved when the CC implementation based on measured displacements on a contour of a subdomain is performed, providing the crack initiation length remains small compared to the subdomain size.

Keywords: Finite fracture mechanics, Digital Image Correlation, small-scale

1. Introduction

Wedge splitting test (WST) [1] consists of the insertion of a wedge in a notched sample. WST is often used in the study of concrete [2] and of refractories with sample dimensions approximately equal to hundreds of millimeters [3] [4], as illustrated in Fig. 1 (a). The wedge acts on two rollers
5 that generate a *mode I* loading, leading to stable crack propagation under imposed displacement. Feilden *et al.* [5] studied ceramic samples at the millimeter scale, using WST. At this scale, WST is slightly different from the apparatus used in [3, 4] since no rollers can be inserted to ensure the *mode I* loading (sse Fig. 1 (b)). Sernicola *et al.* [6] performed *in-situ* WST using a nano-indenter in a scanning electron microscope on SiC single crystal and SiC bi-crystal micro-scale samples
10 machined using a focused ion beam. They observed cracks initiating slightly offset from the notch tip. They correlated this phenomenon with asymmetry in the testing sample and in the sample - nano-indenter alignment, more and more prominent as the sample downsizes. It ultimately increased scattering in results. WST has thus been implemented across the scales, the macro-scale

Variable	name	unit
σ_c	: tensile strength	MPa
σ_{nn}	: opening stress	MPa
σ_{nn}^{ref}	: reference σ_{nn} in Section 3.2	MPa
σ_c^{ref}	: reference value for σ_c	MPa
W	: elastic strain energy	J
\mathcal{G}	: energy release rate	J.m ⁻²
\mathcal{G}_c	: critical energy release rate	J.m ⁻²
\mathcal{G}_{inc}	: incremental energy release rate	J.m ⁻²
$\mathcal{G}_{\text{inc}}^{\text{ref}}$: reference \mathcal{G}_{inc} in Section 3.2	J.m ⁻²
$\mathcal{G}_c^{\text{ref}}$: reference value for \mathcal{G}_c	J.m ⁻²
l	: crack length	mm
l_c	: initiation crack length	mm
\bar{l}	: length maximizing \mathcal{G}_{inc}	mm
l_{arr}	: crack arrest length	mm
l_{exp}	: experimentally observed crack length at a given time step	mm
l_{mat}	: Irwin's length	mm
\mathbf{u}_m	: experimental sought displacement field	μm
U_c	: crack initiation imposed displacement	μm
u_{pm}	: Dirichlet boundary condition to apply in the <i>point method</i>	μm
u_{con}	: Dirichlet boundary condition to apply in the <i>contour method</i>	μm
u_{ap}	: Dirichlet boundary condition to apply in the <i>adjusted point method</i>	μm
u_{ref}	: Dirichlet boundary condition applied in the <i>reference configuration</i>	μm
L	: sample length	mm
H	: sample width	mm
a	: notch width	mm
e	: notch tip radius	mm
B	: sample thickness	mm
δ	: distance between sample free edge and contour in the <i>contour method</i>	mm
F_{init}	: experimental crack initiation force	N

Table 1: List of variables and associated units used in the article.

being subjected to less experimental uncertainty but the micro-scale being able to capture local
15 phenomena, such as single interface delamination. Recently, *in-situ* WST has been instrumented
using digital image correlation (DIC) [7-10]. Coupling the capability of WST to initiate a crack
that propagates stably with displacement field measurement using DIC, fracture parameters [7]
or traction-separation profile [8] can be identified. Several methods exist to model fracture using
WST tests and DIC. The most commonly used is cohesive zone models (CZM). They have been
20 successfully coupled with DIC to determine fracture properties of refractories with sample dimen-
sions in the order of tens of millimeters, both at room [9] and elevated temperatures [10]. Efforts
have been made to study the influence of the DIC acquisition zone on the identified parameters
[11, 12]. Alfano *et al.* [11] studied the influence of temporal and spatial discretization on CZM
parameters identification of a double-cantilever beam test using a global DIC approach. On the one
25 hand, the more pre-fracture images were used in DIC, the enhanced the evaluation of the tensile

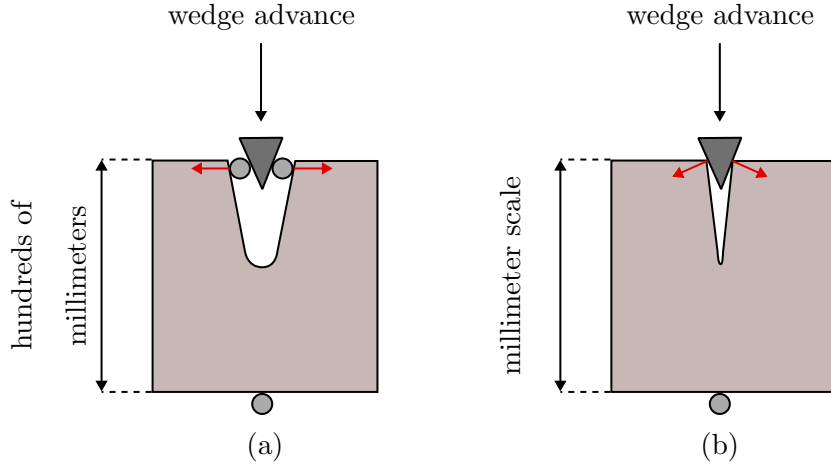


Figure 1: Schematic of (a): WST specimen with dimensions in the range of hundreds of millimeters. The wedge pushes two rollers that generate a *mode I* loading; (b): WST specimen at the millimeter scale with the wedge being in direct contact with the specimen.

strength σ_c was. On the other hand, the estimate of the critical energy release rate \mathcal{G}_c was more accurate, provided more images acquired during stable crack propagation phase were used in DIC. Similarly, the dimensions of the DIC *region of interest* (ROI) have an opposite influence on σ_c and \mathcal{G}_c . Enhanced sensitivity in the estimation of σ_c was observed for smaller ROI, whereas larger ROI gave higher sensitivity to the estimation of \mathcal{G}_c . Rethoré *et al.* [12] studied crazing in PMMA, which is associated with a fracture process zone of tens of micrometers. To adequately capture this phenomenon, DIC data were acquired on a 1 mm^2 zone on a 1000 mm^2 sample surface. As no macroscopic loading information was directly available, crack tip stress intensity factors were extracted [13]. It allowed tracking the position of the crack tip during the test and deriving a traction-opening profile and, thus, determining the cohesive zone parameters. Further use of DIC for fracture parameter or fracture model identification was applied for instance in conjunction to the Boundary Element Method for concrete [14] or with cohesive zone model to identify fracture properties of composites [15] or refractories [16].

CZM are nonlinear models, thus generally time-consuming when employed for fracture property inverse identifications. They require numerous computations before converging towards adequate results [17]. The coupled criterion (CC) [18] is another method to study the initiation and propagation of a crack, thus going beyond classical linear elastic fracture mechanic (LEFM) [19] which can assess crack propagation based on an energy criterion for an infinitesimal crack advance. In a

more general framework, including LEFM, the CC is based on a simultaneous fulfillment of both
45 stress and energy criteria, inducing a finite initiation crack extension. The CC has been successfully
implemented in both 2D [20] and 3D [21]. In addition, it has proven to be a successful method to
study a wide range of crack initiation configurations, *e.g.* mode mixity in elastic isotropic materials
[22] [23], nonlinear material behavior [24], and dynamic crack initiation [25], among others. Under
the assumption of linear elasticity and small deformations, fracture parameter inverse identification
50 using the CC is much faster than using CZM since it only requires some linear elastic finite ele-
ment (FE) computations. The major advantage of the CC is that the fracture parameters are only
required during the post-processing step, which makes the inverse identification procedure numer-
ically efficient. Both CC and CZM fracture parameters inverse identification procedure converge
to similar values [26] [27] provided that the studied material exhibits a brittle behavior at crack
55 initiation. **Fracture parameter identification using the CC generally relies on idealized boundary
conditions of the experiments. Nevertheless, the actual boundary conditions may differ from such
idealized prescribed forces or displacements. The latter can actually be estimated using DIC to
measure the displacement fields at the surface sample during the test and better represent the
loading applied to the specimen.**

60 The objective of this work is to implement the CC using boundary conditions based on displace-
ment fields measured by DIC to determine the tensile strength and critical ERR from WST on
PPMA millimeter-sized samples. The experimental procedure is presented in Section 2. Section
3 presents the CC and its implementation using boundary conditions from displacement fields
measured using DIC. In addition, a parametric study is conducted to determine the methodology
65 limitations of such an approach. Finally, fracture parameters are identified (Section 4).

2. Definition of the test

2.1. Sample preparation

Cast PMMA samples are laser-cut from a 3-mm plate using a Trotec Speedy 100 machine
(Trotec Laser GmbH, Marchtrenk, Austria). Dimensions are given in Table 2, *i.e.* with L , H ,
70 B , e , a and F_{init} being the sample length, width, thickness, notch tip radius, notch width and
experimental force to failure respectively. Narrowest notches (*i.e.* samples S_1 and S_2) are obtained
by specifying a 0 mm notch radius to the machine (*i.e.* induced by the laser spot diameter). Larger

notches (*i.e.* samples S_3 , S_4 , and S_5) are obtained by specifying a 0.15 mm notch radius to the machine. After cutting, a 90°C-120 minutes heat treatment is conducted to relax laser-induced thermal residual stresses. After heat treatment, samples are cooled down in the oven for 12 hours.

Sample	L (mm)	H (mm)	B (mm)	e (μm)	a/H	F_{init} (N)
S_1	8.4	8.5	3.0	86	0.35	69.6
S_2	8.4	8.4	3.0	89	0.35	72.2
S_3	7.2	7.2	2.9	160	0.38	65.3
S_4	7.2	7.2	2.9	150	0.36	64.9
S_5	8.4	8.4	3.0	189.5	0.38	68.0

Table 2: Sample geometrical dimensions and experimental forces at crack initiation.

A freckle is applied to perform DIC. First, a homogeneous white layer is applied using acrylic spray paint. Then, black speckles are deposited using another acrylic spray paint.

2.2. Wedge splitting test

WST is performed using a Microtest 2 kN machine from Deben UK Ltd (London, UK). A homemade module carrying a tungsten carbide wedge is progressively inserted in the sample notch (Fig. 2). To ensure quasi-static loading conditions, a prescribed displacement rate of $33 \mu\text{m}\cdot\text{min}^{-1}$ is applied. Tests are conducted either up to the complete fracture of the sample or 20 seconds after crack initiation. Fig. 3 shows the force-displacement curves for the five tested samples. The material exhibits a linear-elastic behavior up to crack initiation. Crack initiation is followed by unstable crack propagation, both phenomena inducing a sudden force drop. After unstable crack propagation following initiation, the imposed displacement must be increased for further crack propagation, which means that stable crack propagation occurs.

2.3. Digital image correlation

DIC is a contactless technique to measure displacement on a sample surface. Images are acquired over time. Let f be the reference image grey level field, g be the deformed image grey level field, and u be estimations of the searched displacement field \mathbf{u}_m that transforms the deformed image into the reference image. An algorithm is used aiming to minimize the sum of the squared grey

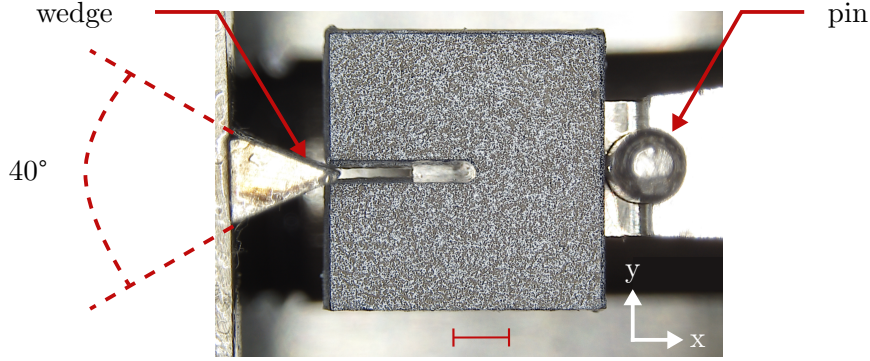


Figure 2: Tested sample, wedge, and pin from the testing apparatus. The scale bar is 1.5 mm long.

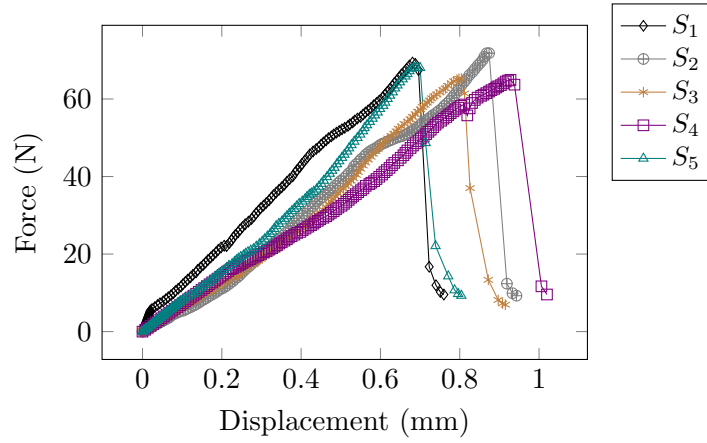


Figure 3: Force-displacement curves for the 5 tested samples.

level difference between the reference image and the deformed image corrected by the displacement field estimation [28]:

$$\mathbf{u}_m = \underset{\mathbf{u}}{\text{Argmin}} \sum_{ROI} [f(\mathbf{x}) - g(\mathbf{x} + \mathbf{u}(\mathbf{x}))]^2, \quad (1)$$

The minimization is performed using a FE-based nonlinear least-squares algorithm with a global
 90 approach implemented in the software *Ufreckles* [29]. The image acquisition device is an **optical**
 microscope (Hirox Japan Co Ltd, Tokyo, Japan) with a 8 μm physical pixel size. Images are ac-
 quired every two seconds.

Undesired acquisition noise is inherent to DIC. This noise is a function of the experimental set-
 95 up, *e.g.* acquisition apparatus, lightning, speckle quality, DIC mesh size, and ROI contour shape.
 This noise is assessed prior to WST by acquiring images of the sample without applying any load.

Consequently, the displacement should be null on the whole sample surface. The maximum error is found to be 0.23 ± 0.06 pixels, or equivalently $1.86 \pm 0.53 \mu\text{m}$. DIC mesh size element equals 50 pixels, or approximately $400 \mu\text{m}$ corresponding to a good trade-off between measurement noise and spatial segmentation. Moreover, to reduce the noise, the DIC FE mesh is taken slightly inside the sample and does not encompass the notch. A structured mesh with 4-node quadrilateral elements is chosen. Examples of displacement and strain fields measured on specimen S_2 are shown in Fig. 4.

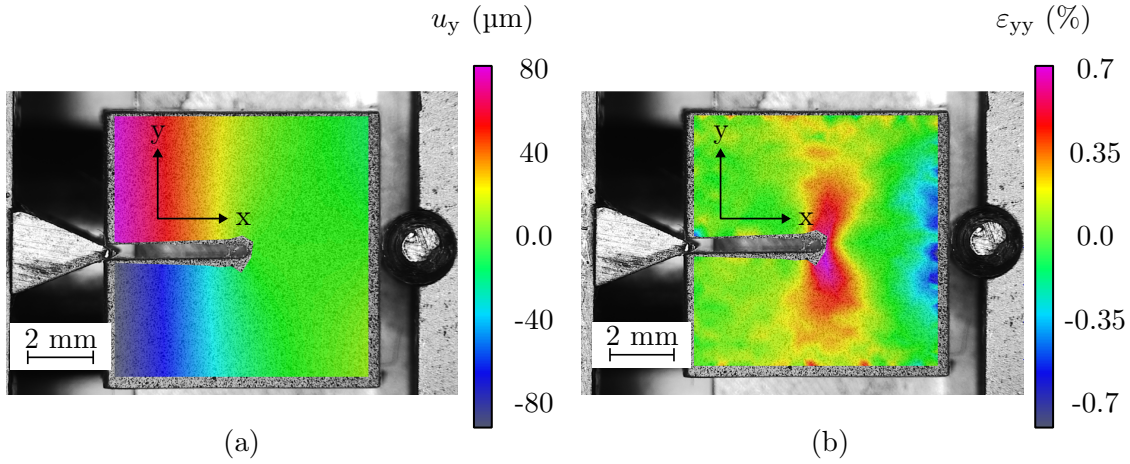


Figure 4: (a): Displacement and (b) strain fields at the surface of specimen S_2 just before crack initiation.

3. DIC-based coupled criterion implementation

3.1. The coupled criterion

The CC is a model dedicated to studying the initiation of a crack. It is based on the simultaneous fulfillment of stress and energy conditions. The stress criterion states the opening stress σ_{nn} must be larger than the material tensile strength σ_c over the whole area corresponding to a putative crack before initiation. The energy criterion requires that the incremental energy release rate (IERR) \mathcal{G}_{inc} , defined as $\frac{-\Delta W}{\ell}$ in 2D, where $\Delta W(\ell)$ is the elastic strain energy variation due to crack opening and ℓ the crack length, must be equal to or larger than the critical energy release rate \mathcal{G}_c . These two conditions write:

$$\begin{cases} \sigma_{\text{nn}}(\ell, \mathbf{U}_c) \geq \sigma_c, & \forall \ell \leq \ell_c, \\ \mathcal{G}_{\text{inc}}(\ell_c, \mathbf{U}_c) \geq \mathcal{G}_c, \end{cases} \quad (2)$$

where ℓ_c is the crack initiation length and U_c is the applied displacement. Fig. 5 schematically shows the variation of \mathcal{G}_{inc} and σ_{nn} as a function of the crack length for a WST. It can be noticed that σ_{nn} decreases with increasing crack length, whereas \mathcal{G}_{inc} first increases before decreasing, thus reaching a unique maximum. Solving the CC reverts to determining the minimum $U_0 = U_c$ for

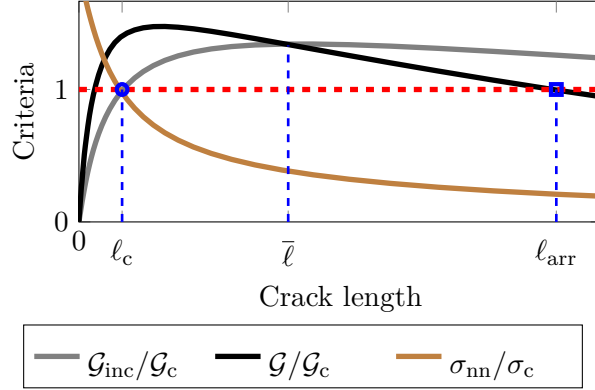


Figure 5: Schematic explanation of the coupled criterion when used with DIC. \mathcal{G}_{inc} and σ_{nn} normalized by their respective critical values as a function of the crack length. As the BC of the FE model corresponds to a situation of crack initiation, each couple $\mathcal{G}_{\text{inc}}-\sigma_{\text{nn}}$ is a possible $\mathcal{G}_c-\sigma_c$ couple if $\ell < \bar{\ell}$. \mathcal{G} and \mathcal{G}_{inc} define the minimum and maximum crack arrest lengths up to which unstable crack propagation happens.

which both conditions given in Eq. 2 are fulfilled for a length corresponding to ℓ_c . As a consequence, the CC predicts that crack initiation occurs as a sudden event with a crack length jumping from 0 to ℓ_c for an imposed displacement U_c . After initiation, the crack propagation can be assessed based on LEFM **using the energy release rate (ERR) \mathcal{G}** . The **stable** crack propagation condition is defined as $\mathcal{G} = \mathcal{G}_c$, with $\mathcal{G} = \frac{-\delta W}{\delta \ell}$. In configurations where \mathcal{G}_{inc} exhibits a maximum, ℓ_c is smaller than or equal to the length maximizing \mathcal{G}_{inc} [30], denoted $\bar{\ell}$ (see Fig. 5). If ℓ_c maximize \mathcal{G}_{inc} , *i.e.* $\ell_c = \bar{\ell}$, after initiation:

$$\begin{cases} \mathcal{G}(\ell_c) &= \mathcal{G}_{\text{inc}}(\ell_c) = \mathcal{G}_c, \\ \frac{d\mathcal{G}(\ell)}{d\ell} < 0 & \forall \ell > \ell_c. \end{cases} \quad (3)$$

As a consequence, stable crack propagation occurs after initiation. Otherwise, if ℓ_c is smaller than $\bar{\ell}$, after initiation:

$$\begin{cases} \mathcal{G}(\ell_c) > \mathcal{G}_{\text{inc}}(\ell_c) = \mathcal{G}_c, \\ \frac{d\mathcal{G}(\ell)}{d\ell} > 0 \end{cases} . \quad (4)$$

It means that unstable crack propagation occurs just after initiation until an arrest length ℓ_{arr} verifying $\mathcal{G}(\ell_{\text{arr}}) = \mathcal{G}_c$, where ℓ_{arr} is the arrest length schematically defined on Fig. 5.

Full-field measurement techniques such as DIC allow to have direct access to the displacement field \mathbf{u}_m , from which FE boundary conditions (BC) can be extracted. The methodology to convert \mathbf{u}_m in FE BC is detailed in Section 3.2. The FE calculation using the BC extracted from DIC thus provides σ_{nn} before initiation, and \mathcal{G}_{inc} as a function of ℓ for the initiation-imposed displacement. As a consequence, three unknowns remain: ℓ_c , σ_c and \mathcal{G}_c . These parameters can be determined since Eq. 2 is fulfilled at crack initiation, which provides $(\mathcal{G}_c, \sigma_c, \ell_c)$ so that:

$$\begin{cases} \sigma_c = \sigma_{nn}(\ell_c), \\ \mathcal{G}_c = \mathcal{G}_{inc}(\ell_c). \end{cases} \quad \text{with } \ell_c \in [0, \bar{\ell}] \quad (5)$$

Only crack lengths from 0 to $\bar{\ell}$ are considered, otherwise, crack initiation at a smaller imposed displacement would be possible [30].

It must be emphasized that Eq. 5 yields an infinite number of admissible fracture parameter couples $(\sigma_c, \mathcal{G}_c)$, corresponding to initiation lengths between 0 and $\bar{\ell}$. As a consequence, the sole knowledge of the initiation loading is not sufficient to determine both the tensile strength and critical energy release rate, which requires additional data. It is not trivial to measure ℓ_c experimentally since, in most configurations, unstable crack propagation follows crack initiation. However, the arrest crack length after unstable crack propagation can be measured experimentally and compared to that obtained using the CC, ℓ_{arr} (see Fig. 5). Finally, the final stable crack propagation can also be used to determine the material critical energy release rate based on LEFM crack propagation condition $\mathcal{G}(\ell_{exp}) = \mathcal{G}_c$, where ℓ_{exp} is the crack length measured experimentally. It is done by calculating the energy release rate using the displacement measured using DIC as BC.

Ultimately, coupling DIC with a full-FE implementation of the CC amounts to:

1. determining all possible $\sigma_c(\ell_c)$ and $\mathcal{G}_c(\ell_c)$ using crack initiation BC determined with DIC in a FE model,
2. computing the associated ℓ_{arr} ,
3. determining \mathcal{G}_c based on stable crack propagation phase,
4. among all possible values determined in 1. and based on results from 2. and 3., determining σ_c and \mathcal{G}_c that best reproduce the initiation loading, arrest crack length and/or stable crack propagation.

3.2. Influence of the boundary conditions

DIC provides the displacement fields at the surface of the specimen, from which BC of the FE model can be determined. In the literature, different approaches are used to extract BC from displacement fields obtained by DIC. The displacement acquired over the contour of a given ROI can be used. Such an approach has been implemented by Fedele *et al.* [31] to determine CZM parameters from a debonding test. The ROI was two orders of magnitude smaller than the corresponding experimental testing sample (*i.e.* ROI dimensions in the order of the millimeter). DIC displacements inside the ROI were incorporated in the material parameter identification algorithm objective function. Similarly, Vargas *et al.* [32] prescribed BC on a ROI contour and compared the resulting displacement field to the full-field results inside the ROI to determine elastic properties using a finite element model updating approach. In both approaches, the BC are applied along a closed contour. Another approach is to apply BC in the FE model at the same position where the testing apparatus applies loading on the testing sample. However, these exact locations might not be encompassed by DIC. To tackle this issue, Vargas *et al.* used a local measurement of WST notch opening displacement to extrapolate the BC [33]. This extrapolation was made after a relationship was established in a previous study [34] between the notch opening displacement (NOD) and the crack mouth opening displacement (CMOD), on a test where both locations were encompassed by DIC. Then, the CMOD was applied as BC. Using such an approach, they identified fracture energies in agreement with reference values from experimentally determined work of fracture.

To assess the influence of the type of BC on the determination of fracture parameters, a parameter study is conducted. Three different BC application methodologies are tested, namely:

- the *point method* is the direct application of \mathbf{u}_{pm} , the displacement at the contact between the testing apparatus and the sample. This displacement is directly measured from the DIC displacement (see Fig. 6 - a).
- the *contour method* consists of applying BC along a contour taken inside the sample, near the sample free edges. This displacement data is denoted \mathbf{u}_{con} . The BC are directly extracted from DIC. The contour is defined by a parameter δ , which defines the distance of the contour from the sample outer edges.

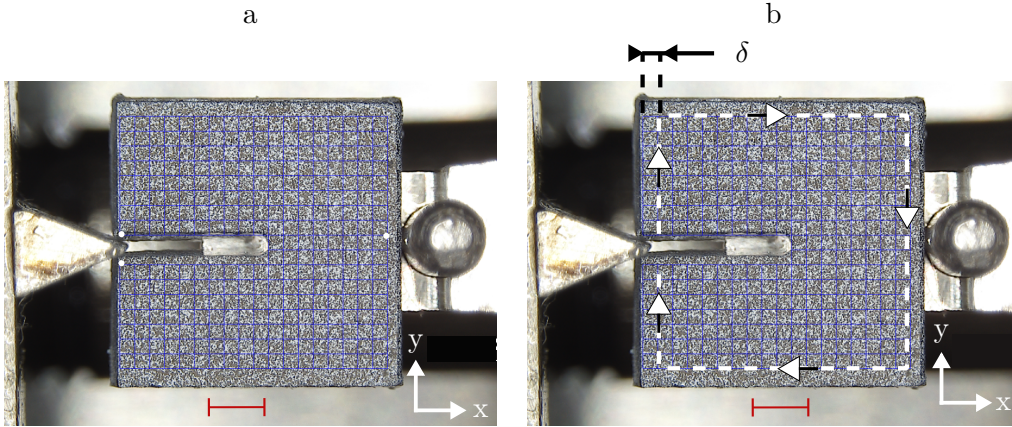


Figure 6: Graphical illustration of: (a) the *point method* boundary condition extraction, where the three white points represent the location where BC are extracted. (b) the *contour method* boundary condition extraction. The exact displacement values are taken at DIC mesh nodes along a contour that encompasses the notch (dashed white line). Polynomial interpolations convert these discrete values into a continuous contour displacement.

- the *adjusted point method (AP method)* is the BC application of a displacement \mathbf{u}_{ap} at the contact between the sample and the apparatus, *i.e.* as for \mathbf{u}_{pm} . However, \mathbf{u}_{ap} differs from \mathbf{u}_{pm} , since a gradient descent algorithm is used to determine the value of \mathbf{u}_{ap} that results in a contour displacement as close as possible from \mathbf{u}_{con} .

160 The reliability of the three methods is evaluated by generating virtual experimental data from a numerical FE simulation. A point displacement \mathbf{u}_{ref} is imposed at the contact location between the wedge and the specimen, which enables calculating σ_{nn} and \mathcal{G}_{inc} that will be considered as reference values for the analysis. These values will thus be referred to as $\sigma_{\text{nn}}^{\text{ref}}$ and $\mathcal{G}_{\text{inc}}^{\text{ref}}$.

3.2.1. Point method

165 In the absence of DIC acquisition noise, *point method* should provide the actual displacement at the contact between the wedge and the specimen. DIC acquisition noise has been estimated as explained in Section 2.3. In addition to DIC noise, an error can be committed on wedge-specimen contact coordinate identification from DIC data. Wrong identification of the contact zone can cause an error up to 0.4 pixels, or 3.2 μm , *i.e.* twice the DIC acquisition noise. There is no acquisition
170 noise in the virtual experiments, thus the point method provides the reference configuration.

3.2.2. Contour method

In the current section, the influence of the choice of contour is assessed. Different contours are extracted from the reference configuration, with varying δ (see Section 3.2). Then, gaussian noise is added to the displacement on the contour. The normal distribution associated with this noise exhibits a mean value of 0 and a standard deviation equal to 2 %, which is the ratio between the DIC acquisition noise (see Section 2) and the maximum observed opening displacement. The resulting displacement is applied as BC in different simulations. The opening stress and incremental energy release rate are computed. Fig. 7 shows the variation of $\frac{|\mathcal{G}_{\text{inc}} - \mathcal{G}_{\text{inc}}^{\text{ref}}|}{\max(\mathcal{G}_{\text{inc}}^{\text{ref}})}$ and $\frac{|\sigma_{\text{nn}} - \sigma_{\text{nn}}^{\text{ref}}|}{\max(\sigma_{\text{nn}}^{\text{ref}})}$ for increasing δ , *i.e.* for a contour defined further and further from the specimen free edges. In this figure, the crack length is normalized by the maximum computationally admissible crack length, *i.e.* $W - a - \delta$ (see Section 2 for definitions of a and δ).

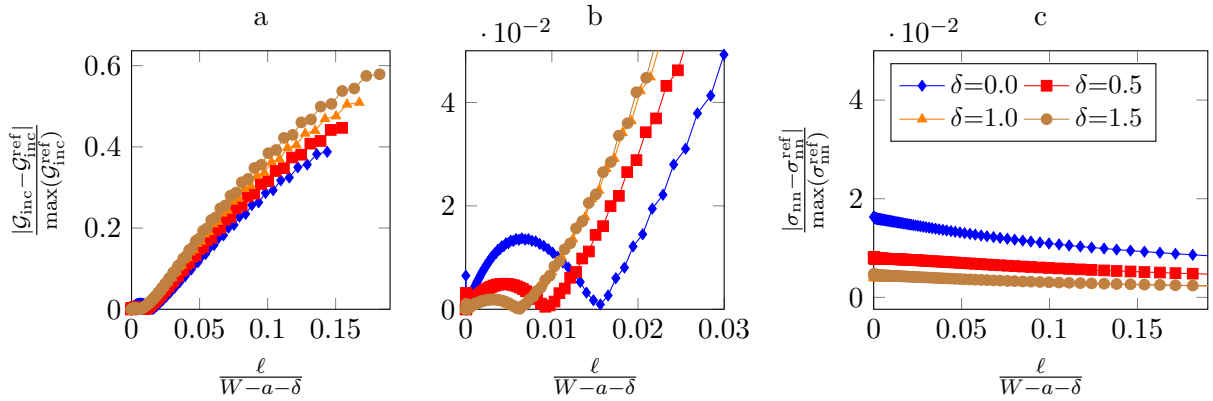


Figure 7: Variation of (a-b) the IEER and (c) the stress relative error as a function of the normalized crack length for different contour sizes, with a zoomed view on errors below 5 %.

The computation of σ_{nn} is in good agreement with the reference configuration (Fig. 7 - c). It can be observed a slight influence of δ on the opening stress, even though the maximum relative observed error, *i.e.* for short crack lengths and $\delta = 0.0$ is only 1.8 %. The error made on \mathcal{G}_{inc} is larger, as shown on Fig. 7 - a & b. Indeed, the relative error becomes larger than 5 % as soon as $\frac{\ell}{W-a-\delta} > 0.02$. Moreover, it can be noticed that contrary to $\frac{|\sigma_{\text{nn}} - \sigma_{\text{nn}}^{\text{ref}}|}{\max(\sigma_{\text{nn}}^{\text{ref}})}$ where deviation from the reference values decreases with increasing δ , deviation of $\frac{|\mathcal{G}_{\text{inc}} - \mathcal{G}_{\text{inc}}^{\text{ref}}|}{\max(\mathcal{G}_{\text{inc}}^{\text{ref}})}$ is larger when δ is increases, *i.e.* when the subdomain size becomes smaller.

Consequently, using the *contour method*, CC resolution is expected to remain accurate for crack

190 length smaller than 2 % of the sample ligament. As explained in Section 3.1, provided that full-field data are acquired at crack initiation (thus fulfilling the CC), FE model allows the determination of σ_c - \mathcal{G}_c corresponding to ℓ_c smaller than $\bar{\ell}$. Fig. 8 shows the evolution of $\frac{\ell_c}{W-a-\delta}$ as a function of Irwin's length $\frac{E'\mathcal{G}_c}{\sigma_c^2}$ with $E' = \frac{E}{1-\nu^2}$. The critical value $\frac{\ell_c}{W-a-\delta} = 0.02$ corresponds to $\ell_{\text{mat}} \approx 2$ mm, with Young's modulus E and Poisson's ration ν equal to 2200 MPa and 0.37 respectively. The
 195 inequality $\ell_{\text{mat}} < 2$ mm assesses that no methodological bias comes from the *contour method* in the study of crack initiation from full-field data. ℓ_{mat} is *a priori* unknown for the PMMA under study since \mathcal{G}_c and σ_c are both to be determined. However, it is in the range of tens of μm [26].

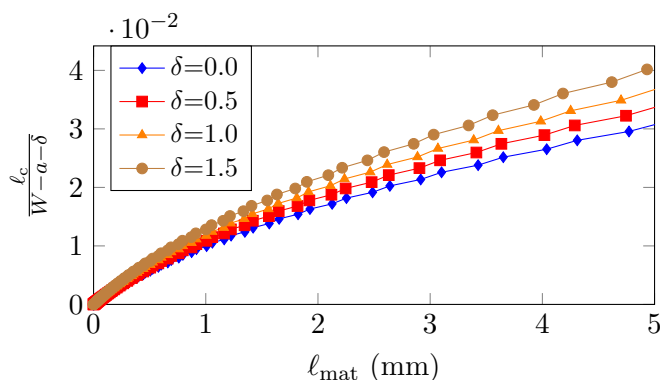


Figure 8: Evolution of the normalized critical crack length $\frac{\ell_c}{W-a-\delta}$ as a function of ℓ_{mat} .

3.2.3. Adjusted point method

To assess the efficiency of the *AP method*, the displacement applied in the reference configura-
 200 tion is corrupted by noise following a normal law with a standard deviation equal to 12.5 %, which overestimates the actual error. Note that virtual tests were also conducted with a noise having a standard deviation similar to the one applied when assessing the *contour method* noise robustness, see Section 3.2.2. For this noise level both $\frac{G_{\text{inc}}}{G_{\text{inc}}^{\text{ref}}}$ and $\frac{\sigma_{\text{nn}}}{\sigma_{\text{nn}}^{\text{ref}}}$ were below $5 \cdot 10^{-3}$. This value is chosen to assess the efficiency of the method. The resulting displacement along a contour as defined for the
 205 *contour method* is extracted. Then, the input displacement is iteratively adjusted using a gradient descent algorithm to minimize in a least-squares sense the difference of the displacement taken along the contour when the reference and corrupted BC are applied. This procedure is repeated 5 times to evaluate statistical effects. Fig. 9 shows $\frac{G_{\text{inc}}}{G_{\text{inc}}^{\text{ref}}}$ and $\frac{\sigma_{\text{nn}}}{\sigma_{\text{nn}}^{\text{ref}}}$ as the function of $\frac{\ell}{W-a-\delta}$ for one of the tests. The presented configuration is the one showing the highest deviation with respect to

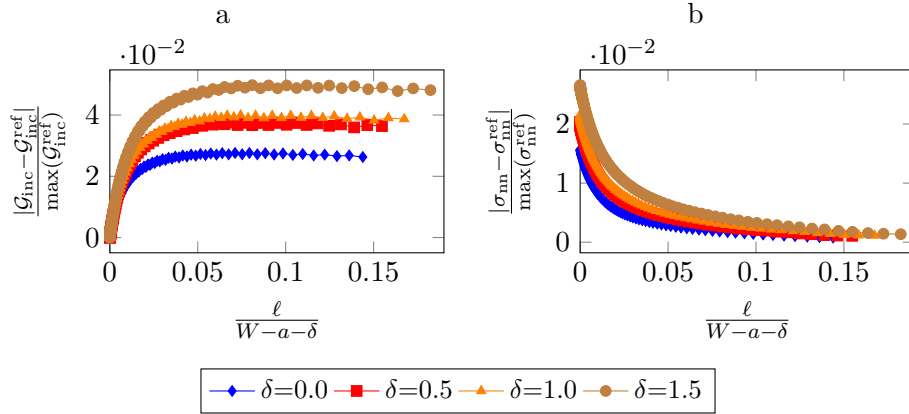


Figure 9: Assessment of the *AP method* in the computation of (a) $\frac{G_{inc}}{G_{inc}^{ref}}$ and (b) $\frac{\sigma_{nn}}{\sigma_{nn}^{ref}}$.

210 the reference. Nevertheless, both the $\frac{G_{inc}}{G_{inc}^{ref}}$ and $\frac{\sigma_{nn}}{\sigma_{nn}^{ref}}$ are less than 5 % different from the reference values, whatever the crack length.

4. Fracture property identification

In the present section, the three methods depicted in Section 3 for fracture parameter identification are compared on five experimental WST (sample geometries given in Table 2).

215 4.1. Reference configuration

To compare the methods relying on the use of DIC BC in a FE model, reference values for \mathcal{G}_c and σ_c are first determined from 3PB tests on notched (SENB) and plain beams. The dimensions of the plain beams can be found in Table 3, whereas SENB dimensions are given in Table 4. The bending sample dimensions are close to the WST sample dimensions, allowing to perform the
 220 bending tests with the same load cell and the same loading rate. For each testing sample type, an inverse identification routine based on the CC is conducted (see [35] for methodology details) leading to different \mathcal{G}_c - σ_c relationships. The reference values \mathcal{G}_c^{ref} and σ_c^{ref} are determined as the values fulfilling both relationships from plain and SENB samples. The \mathcal{G}_c - σ_c relationships obtained for each specimen evidence experimental scattering, thus an average \mathcal{G}_c - σ_c relationship is calculated
 225 among all samples of a given geometry. It gives $\mathcal{G}_c^{ref} = 318 \pm 77 \text{ J.m}^{-2}$, and $\sigma_c^{ref} = 116 \pm 5 \text{ MPa}$.

Sample	L (mm)	W (mm)	B (mm)	F_{init} (N)
$3PB_1$	14.95	4.3	2.91	438
$3PB_2$	15.06	3.2	2.95	417

Table 3: Sample geometrical dimensions and force to failure for plain specimens in bending.

Sample	L (mm)	W (mm)	B (mm)	e (mm)	F_{init} (N)
$3PB_1^n$	14.8	3.49	2.90	0.594	46
$3PB_2^n$	14.95	3.54	2.90	0.604	52
$3PB_3^n$	15.07	3.2	2.97	0.692	58

Table 4: Sample geometrical dimensions and force to failure for notched specimens in bending.

4.2. Crack process

The DIC data can be divided into four categories: in the linear elastic regime, at crack initiation, during unstable crack propagation that follows crack initiation, and finally during stable crack propagation, if any. The presence of stable crack propagation is required to identify a single \mathcal{G}_c value (see Section 3). The transition between unstable and stable crack propagation can be arduous to determine optically. Consequently, for each DIC frame after crack initiation, FE simulations are conducted to determine \mathcal{G}_c from crack propagation. **Similarly to FE simulations for crack initiation assessment, the BC are extracted from the displacement fields measured using DIC on a contour and the corresponding ERR is calculated. Since stable crack propagation occurs at this stage, the obtained ERR provides an estimate of the material critical ERR.** Fig. 10 (a) shows the evolution of ℓ_{exp} and the associated $\mathcal{G}_c(\ell_{\text{exp}})$ determined from crack propagation for the *contour method* for samples S_2 (small notch radius) and S_3 (large notch radius). Stable crack propagation starts when \mathcal{G}_c does not vary over time. Consequently, for each sample, \mathcal{G}_c is determined as the average of all values determined for times corresponding to stable crack propagation. The comparison between *contour*, *point* and *AP methods* for sample S_5 is shown in Fig. 10 (b), where it can be seen that the methods do not converge towards the same \mathcal{G}_c values, with a maximum difference between all methods equals to 30 J.m^{-2} . The red hatched zone on Fig. 10 (b) corresponds to unstable crack propagation, where $\mathcal{G} > \mathcal{G}_c$.

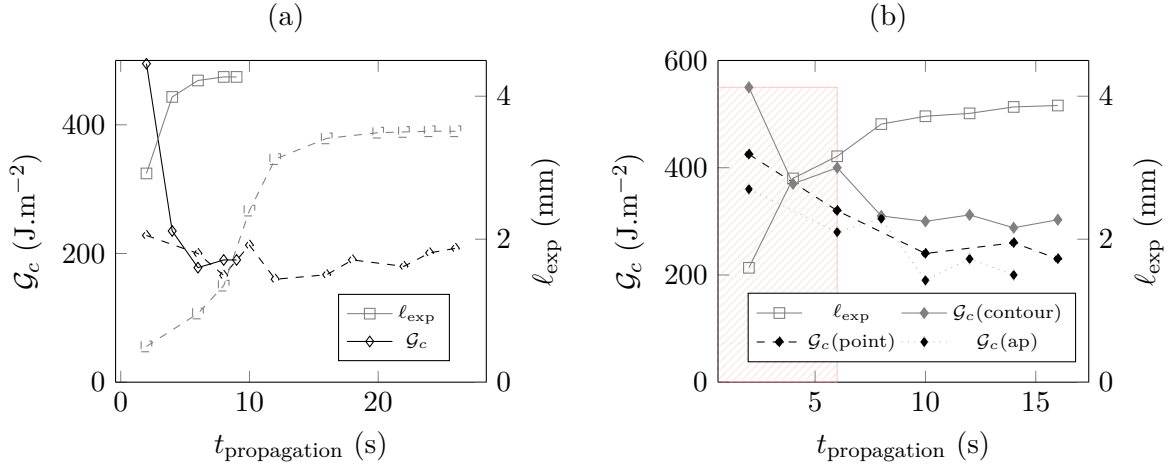


Figure 10: (a) Evolution of \mathcal{G}_c and l_{exp} with time after crack initiation computed with the *contour method* for samples S_2 and S_3 , in solid and dashed line respectively. (b) Comparison of the computation of \mathcal{G}_c on sample S_5 for the *contour* and *point methods*.

245 4.3. Point Method

Results from *point method* parameter identification are shown in Fig. 11 - a. The diamond markers show the \mathcal{G}_c values determined with stable crack propagation BC. The *point method* gives $\mathcal{G}_c = 324 \pm 84 \text{ J.m}^{-2}$ and $\sigma_c = 40 \pm 22 \text{ MPa}$, see the green hatched rectangle on Fig. 11 - a. For sample S_3 , \mathcal{G}_c equals 400 J.m^{-2} . For this value, the CC does not predict crack initiation, thus, no σ_c can be determined. The determined strength value strongly diverges from the tensile strength value estimated with 3PB (*i.e.* relative error of -59%). However, stable crack propagation is adequately modeled with the *point method*, as the error lies below 2 %. Computing the crack arrest lengths linked to \mathcal{G}_{inc} and \mathcal{G} determined at crack initiation also allows to define upper and lower bounds for \mathcal{G}_c as explained in Section 3.1. The computation of \mathcal{G} from crack initiation gives $\mathcal{G}_c(l_{arr})$ equal to half the reference value.

4.4. Contour Method

An example of applied displacement u^{con_x} and u^{con_y} (see Fig. 6 for the axis definition) at crack initiation with $\delta = 0.5 \text{ mm}$ can be found on Fig. 12 - a & b respectively. It can be noted that u^{con_x} is not symmetric. It could be caused by misalignment of the sample with respect to the testing apparatus, or imperfection in the notch laser cutting process. Effect of asymmetry has been checked and appears to be insignificant on the identified \mathcal{G}_c and σ_c , as fracture is mode-I dominated, and

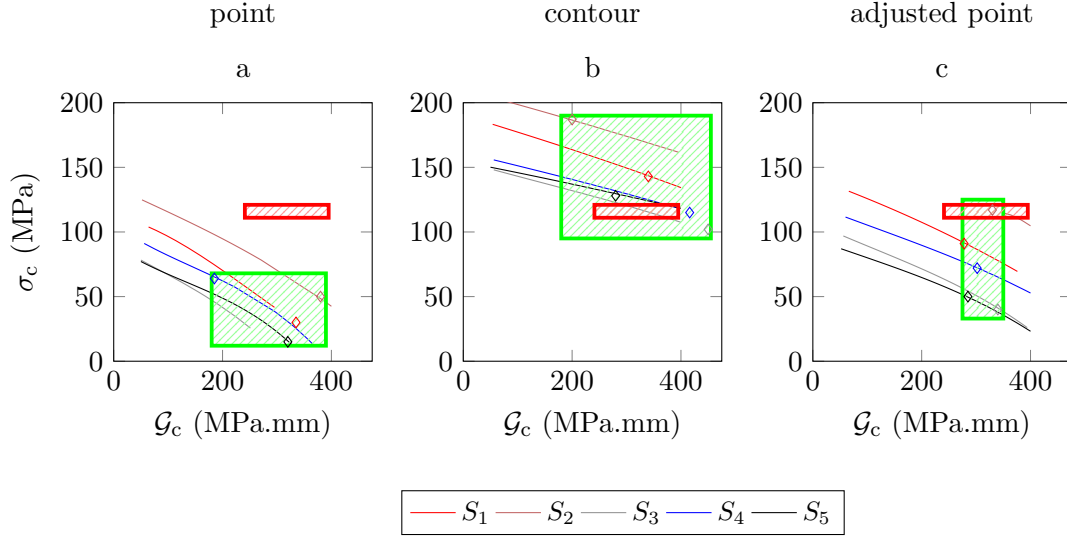


Figure 11: Parameter identification results. Solid lines depict the results obtained from studying the crack initiation. The unique value extracted from the crack propagation study is depicted with a diamond marker. The green hatched zones represent the identified \mathcal{G}_c and σ_c for each method, *i.e.* **maximum and minimum** values. The reference values are represented by the red-hatched zones.

thus the effect of u^{con_y} dominates over u_{con_x} . Results from the fracture parameter identification using the *contour method* are presented in Fig. 11 - b. This method gives $\mathcal{G}_c = 337 \pm 101 \text{ J.m}^{-2}$ and $\sigma_c = 135 \pm 32 \text{ MPa}$, see the green hatched rectangle on Fig. 11 - b. As for the *point method*, the *contour method* allows for an acceptable determination of \mathcal{G}_c (*i.e.* relative error of 6 %). However, the *contour method* identifies a strength value with a relative error of 16 %, which is almost 4 times lower than the error committed using the *point method*. This behavior can be explained by the displacement field on the surface sample, and especially the displacement observed near the wedge-sample contact. Fig 13 shows the displacement along a predefined contour. Solid lines represent the opening displacement (*i.e.* u^{con_y}) for the *contour method*, whereas dashed lines represent the displacement along the same contour obtained applying the *point method*. Fig. 13 - a presents the displacement at crack initiation, whereas Fig. 13 - b presents results obtained during stable crack propagation. It can be observed that pointwise application of the BC results in a similar displacement to the displacement extracted from DIC during stable crack propagation. However, pointwise techniques fail to mimic the displacement from DIC at crack initiation. Indeed, Fig. 13 - a shows a linear decrease of u^{con_y} for curvilinear abscissa increasing from 0 to 5 mm, see red circle

in Fig. 12, that cannot be obtained with either the *point* or the *AP* method. This difference could be explained by viscous effects that are disregarded. Computation of \mathcal{G}_c from crack initiation

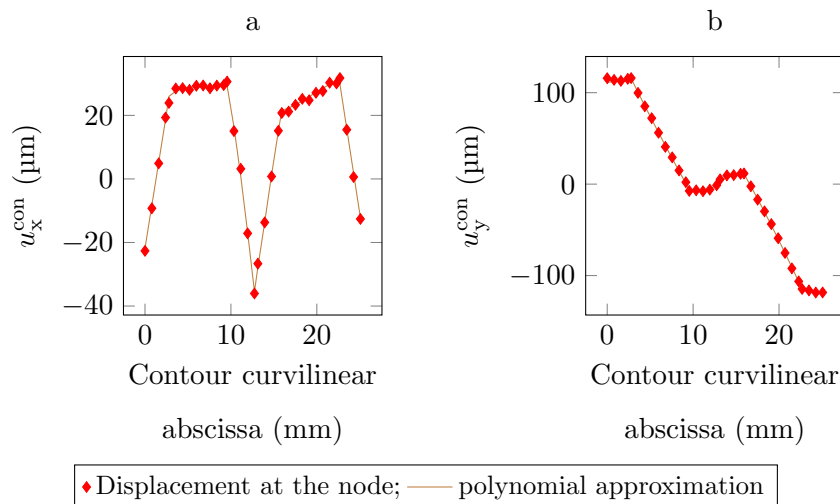


Figure 12: Displacement along S_4 contour for $\delta = 0.5$ mm.

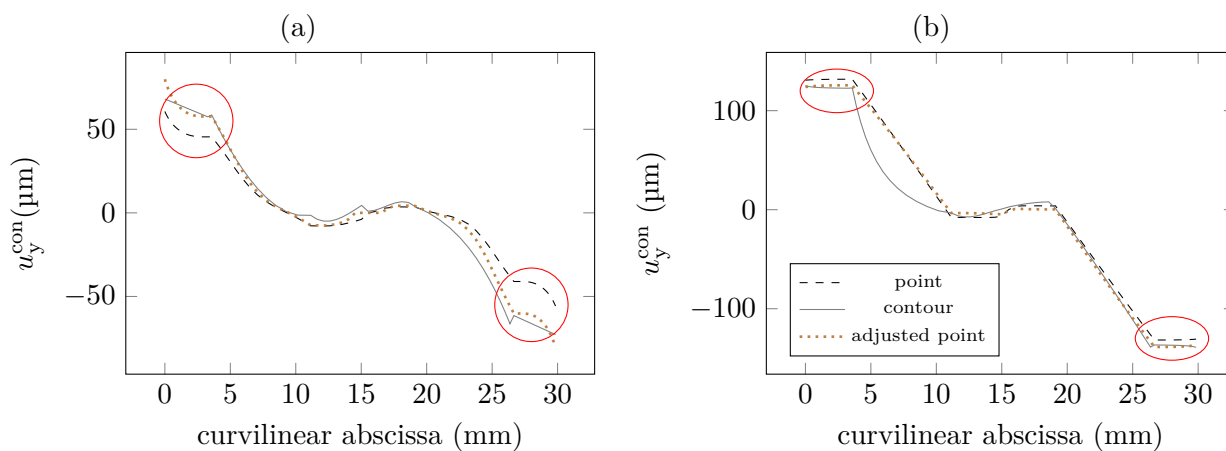


Figure 13: Displacement applied as BC in *contour method* (solid line), displacement along the same contour resulting from *point method* (dashed line) and *AP method* (dotted line), (a) at crack initiation; (b) during stable crack propagation.

gives an incremental energy release rate one order of magnitude below the reference \mathcal{G}_c .

280 4.5. Adjusted point method

It can be observed from Fig. 13 that the *AP method* results in a contour displacement closer to the one from the *contour method* with respect to the *point method*. The *AP method* gives $307 \pm 23 \text{ J.m}^{-2}$ and $74 \pm 28 \text{ MPa}$ for \mathcal{G}_c and σ_c respectively (see the green hatched rectangle on Fig. 11 - c), which corresponds to relative errors of -3 % and -36 % respectively as compared to the
285 reference values identified in bending. For similar reasons as the *point method* (see Section 4.3), the *AP method* fails to predict accurately the strength. However, the *AP method* gives a better \mathcal{G}_c determination with respect to the two other methods, by reducing the scattering in the results. As for the *point method*, \mathcal{G}_c determined from crack initiation is half the reference value.

5. Discussion

290 5.1. Influence of the sample geometry

Two sets of notch radii have been tested (see Table 2). Under the present testing condition, this difference in notch radii does not have an influence on F_{init} . It seems, however, to have an influence on the determination of fracture parameters when crack initiation BC are applied. Indeed, Fig. 11 - a, b, c show that the values determined for samples with larger notch radii (S_3, S_4, S_5) are
295 systematically lower than values determined for samples with smaller notch radii. As the notch radius difference is accounted for in the FE models, fracture parameter identification should be insensitive to this parameter. Thus, this difference might be explained by the FE model, which does not account for the presence of a process zone ahead of the notch tip. Moreover, this difference might also emphasize a limitation of the 2D model, *i.e.* the measured BC may not be constant
300 along the sample thickness, and/or the laser cutting process may have resulted in non-parallel faces. It is in agreement with results reported by Vargas *et al.* [33]. They reported a 10 % variation in the computation of \mathcal{G}_c and σ_c if evaluated from the front or the back face on centimeter size refractories using DIC, WST, and CZM. The testing apparatus used in the present study does not allow for *in-situ* image acquisition on both faces. The determination of σ_c considering only samples with
305 small notch radius and using the *contour method* gives a relative error on the strength of 3 %. It is 10 times lower than the error committed when considering samples with a big notch radius. Nevertheless, the difference in notch radii does not have an influence on \mathcal{G} computed with BC taken from stable crack propagation.

5.2. Full-field data

310 Virtual experiments performed in Section 3 enabled determining the validity of the different approaches tested to apply boundary conditions. Defining BC by extracting displacements over a contour remains valid to calculate the stress and the IERR provided the crack length remains small with respect to the contour width. Otherwise, the applied BC provides an erroneous estimate of the IERR and ERR. As a consequence, the *contour method* based on the displacement field measured by
315 DIC just before initiation is accurate for crack initiation assessment since the obtained initiation crack length is small. Nevertheless, the crack arrest length cannot be estimated using the BC based on the displacement field measured just before initiation but requires using the displacement field measured after unstable crack propagation following initiation. The difference in fracture properties obtained using either the *point* or *adjusted point methods* compared to the reference
320 fracture properties may indicate that the way the BC are applied in these FE models is not representative of the actual BC applied to the specimen. As a consequence, the choice of the applied BC appears to be crucial for inverse identification of fracture properties based on crack initiation results. A way to better estimate the BC would consist in measuring the displacement fields on the two opposite specimen surfaces, as sample asymmetry (possibly arising from the
325 sample cutting process) or misalignment of the sample with respect to the wedge and the pin (see Fig. 2) could induce a non-constant displacement variation through the sample thickness.

5.3. Comparison between the methods

Table 5 sums up the identified parameters from the different methods. Among all methods, the
330 *contour method* provides the best agreement with the reference values. The *adjusted point method* improves the *point method* as it gives more reliable results on the determination of σ_c , even though the determined value is lower than the reference one. It should be noted that the *AP method* decreases the dispersion of the results with respect to the other methods, especially on the critical incremental energy release rate.

335 6. Conclusion

Boundary conditions from displacement fields measured by DIC during a WST can be implemented by a pointwise application at the wedge-specimen contact location or through application

Method	σ_c (MPa)	\mathcal{G}_c (J.m ⁻²)
<i>3PB</i>	116 ± 5	318 ± 77
<i>point</i>	48 ± 36	324 ± 84
<i>contour</i>	135 ± 31	337 ± 92
<i>adjusted point</i>	74 ± 28	307 ± 23

Table 5: Couples σ_c - \mathcal{G}_c identified for all the presented methods.

at the contour of a subdomain. While there is no *a priori* crack size limitation for the former, the latter is valid provided the initiation length remains small enough compared to the subdomain size. Based on the measured BC just before crack initiation, the CC provides admissible strength and critical ERR couples corresponding to initiation lengths smaller than the initiation length maximizing the incremental ERR. Among these admissible fracture properties, the optimal couple can be selected by measuring the critical ERR during stable crack propagation. Both pointwise or contour BC application provides critical ERR estimate close to that measured based on three-point bending specimen testing. The contour BC application also provides an accurate estimate of the material tensile strength, whereas it is underestimated using a pointwise BC application. **Finally, an accurate modeling of boundary conditions seems to be of primary importance for a reliable determination of fracture parameters using the CC.**

Acknowledgement

This work was supported by the LABEX MANUTECH-SISE (ANR-10-LABX-0075) of Université de Lyon, within the program "Investissements d'Avenir" (ANR-11-IDEX-0007) operated by the French National Research Agency (ANR). Moreover, we thank the French Ministry of Education and Research for funding this work, through a PhD scholarship. Finally, we thank the GM-Factory (Univ Lyon, INSA Lyon) for laser-cutting our sample.

References

- [1] Brühwiler, E., Wittmann, F., 1990. The wedge splitting test, a new method of performing stable fracture mechanics tests. *Engineering Fracture Mechanics* 35, 117–125. [https://doi.org/10.1016/0013-7944\(90\)90189-N](https://doi.org/10.1016/0013-7944(90)90189-N)

- [2] Guan, J.F., Hu, X.Z., Xie, C.P., Li, Q.B., Wu, Z.M., 2018. Wedge-splitting tests for tensile strength and fracture toughness of concrete. *Theoretical and Applied Fracture Mechanics* 93, 263–275.
360 <https://doi.org/10.1016/j.tafmec.2017.09.006>
- [3] Brochen, E., Dannert, C., Paul, J., Krause, O., 2022. Investigation of fracture behavior of typical refractory materials up to service temperatures. *International Journal of Ceramic Engineering and Science* 4, 68–76.
<https://doi.org/10.1002/ces2.10123>
- [4] Yu, R., Li, G., Zhang, L., Zhou, J., Zhao, S., Zhao, Z., Liu, P., Zhang, X., Pan, L., 2022. Fracture behavior of Al₂O₃-SiO₂ castables by the wedge splitting test and digital image correlation technique. *Ceramics International* 48, 6148–6156. <https://doi.org/10.1016/j.ceramint.2021.11.154>
365
- [5] Feilden, Ezra, Claudio Ferraro, Qinghua Zhang, Esther García-Tuñón, Eleonora D’Elia, Finn Giuliani, Luc Vandeperre, et Eduardo Saiz. « 3D Printing Bioinspired Ceramic Composites ». *Scientific Reports* 7, 1 (23 octobre 2017): 13759. <https://doi.org/10.1038/s41598-017-14236-9>.
- [6] Sernicola, Giorgio, Tommaso Giovannini, Punit Patel, James R. Kermode, Daniel S. Balint, T. Ben Britton, et Finn Giuliani. « In Situ Stable Crack Growth at the Micron Scale ». *Nature Communications* 8, 1 (décembre 2017): 108. <https://doi.org/10.1038/s41467-017-00139-w>.
370
- [7] Doitrand, A., Estevez, R., Thibault, M., Leplay, P., 2020. Fracture and Cohesive Parameter Identification of Refractories by Digital Image Correlation Up to 1200°C. *Exp Mech* 60, 577–590. <https://doi.org/10.1007/s11340-020-00584-7>
375
- [8] Mathieu, F., Hild, F., Roux, S., 2012. Identification of a crack propagation law by digital image correlation. *International Journal of Fatigue* 36, 146–154. <https://doi.org/10.1016/j.ijfatigue.2011.08.004>
- [9] Vargas, R, J. Neggens, R B Canto, J A Rodrigues, et François Hild. « Analysis of a castable refractory using the wedge splitting test and cohesive zone model ». *Journal of the European Ceramic Society* 39, 13 (2019): 3903
380 14. <https://doi.org/10.1016/j.jeurceramsoc.2019.03.009>.
- [10] Doitrand, Aurélien, R. Estevez, M. Thibault, et P. Leplay. « Fracture and Cohesive Parameter Identification of Refractories by Digital Image Correlation Up to 1200°C ». *Experimental Mechanics*, mars 2020, 577–90. <https://doi.org/10.1007/s11340-020-00584-7>.
- [11] Alfano, Marco, Gilles Lubineau, et Glaucio H. Paulino. « Global Sensitivity Analysis in the Identification of Cohesive Models Using Full-Field Kinematic Data ». *International Journal of Solids and Structures* 55 (mars 2015): 66–78. <https://doi.org/10.1016/j.ijsolstr.2014.06.006>.
385
- [12] Réthoré, Julien, and R. Estevez. « Identification of a cohesive zone model from digital images at the micron-scale ». *Journal of the Mechanics and Physics of Solids* 61, 6 (2013): 1407–20. <https://doi.org/10.1016/j.jmps.2013.01.011>.
- [13] Hild, François, and Stéphane Roux. « Measuring stress intensity factors with a camera: Integrated digital image correlation (I-DIC) ». *Comptes Rendus Mécanique* 334 (2006): 8–12. <https://doi.org/10.1016/j.crme.2005.11.002>.
390
- [14] Ferreira M., Venturini W. and Hild F. « On the analysis of notched concrete beams: From measurement with digital image correlation to identification with boundary element method of a cohesive model ». *Engineering Fracture Mechanics* 78(1) (2011) , 71–84.
- [15] Shen B. and Paulino GH. « Identification of cohesive zone model and elastic parameters of fiber-reinforced
395

cementitious composites using digital image correlation and a hybrid inverse technique ». *Cement and Concrete Composites* 33(5) (2011), 572–585.

[16] Vargas R., Canto RB. and Hild F. « Cohesive properties of refractory castable at 600°. Effect of sintering and testing temperature ». *Journal of the European Ceramic Society* 42(14) (2022), 6733–49.

400 [17] Khosrozadeh, Amirali, Amir Khosravifard, et Iraj Rajabi. « Inverse identification of material constants of various cohesive laws for delamination of composites using experimental results ». *Composite Structures*, 3 octobre 2022, 116241. <https://doi.org/10.1016/j.compstruct.2022.116241>.

[18] Leguillon, Dominique. « Strength or toughness? A criterion for crack onset at a notch ». *European Journal of Mechanics - A/Solids*, 2002.

405 [19] Griffith, A.A., 1921. VI. The phenomena of rupture and flow in solids. *Phil. Trans. R. Soc. Lond. A* 221, 163–198. doi:10.1098/rsta.1921.0006

[20] Martin, E., D. Leguillon, A. Catapano, et N. Carrère. « Prediction of Interfacial Debonding between Stiff Spherical Particles and a Soft Matrix with the Coupled Criterion ». *Theoretical and Applied Fracture Mechanics* 109 (octobre 2020): 102749. <https://doi.org/10.1016/j.tafmec.2020.102749>.

410 [21] Doitrand, Aurélien, et Dominique Leguillon. « 3D Application of the Coupled Criterion to Crack Initiation Prediction in Epoxy/Aluminum Specimens under Four Point Bending ». *International Journal of Solids and Structures* 143 (juin 2018): 175–82. <https://doi.org/10.1016/j.ijsolstr.2018.03.005>.

[22] Yosibash, Zohar, Elad Priel, et Dominique Leguillon. « A Failure Criterion for Brittle Elastic Materials under Mixed-Mode Loading ». *International Journal of Fracture* 141, 1–2 (septembre 2006): 291–312. <https://doi.org/10.1007/s10704-006-0083-6>.

415 [23] Sapora, A., et P. Cornetti. « Crack Onset and Propagation Stability from a Circular Hole under Biaxial Loading ». *International Journal of Fracture* 214, 1 (novembre 2018): 97–104. <https://doi.org/10.1007/s10704-018-0315-6>.

[24] Doitrand, Aurélien, et Alberto Sapora. « Nonlinear Implementation of Finite Fracture Mechanics: A Case Study on Notched Brazilian Disk Samples ». *International Journal of Nonlinear Mechanics* 119 (mars 2020): 103245. <https://doi.org/10.1016/j.ijnonlinmec.2019.103245>.

420 [25] Doitrand, Aurélien, Gergely Molnár, Dominique Leguillon, Eric Martin, et Nicolas Carrère. « Dynamic Crack Initiation Assessment with the Coupled Criterion ». *European Journal of Mechanics - A/Solids* 93 (mai 2022): 104483. <https://doi.org/10.1016/j.euromechsol.2021.104483>.

425 [26] Doitrand, Aurélien, Rafael Estevez, et Dominique Leguillon. « Comparison between Cohesive Zone and Coupled Criterion Modeling of Crack Initiation in Rhombus Hole Specimens under Quasi-Static Compression ». *Theoretical and Applied Fracture Mechanics* 99 (février 2019): 51–59. <https://doi.org/10.1016/j.tafmec.2018.11.007>.

[27] Martin, Eric, Thomas Vandellos, Dominique Leguillon, et Nicolas Carrère. « Initiation of Edge Debonding: Coupled Criterion versus Cohesive Zone Model ». *International Journal of Fracture* 199, 2 (juin 2016): 157–68. <https://doi.org/10.1007/s10704-016-0101-2>.

430 [28] Hild, François, Amine Bouterf, et Stéphane Roux. « Damage Measurements via DIC ». *International Journal of Fracture*, IJF at 50, 191, 1–2 (2015): 77–105. <https://doi.org/10.1007/s10704-015-0004-7>.

[29] Rethoré, Julien. « UFreckles ». Zenodo, 1 octobre 2018. <https://doi.org/10.5281/ZENODO.1433776>.

[30] Weißgraeber, P., S. Hell, et W. Becker. « Crack Nucleation in Negative Geometries ». *Engineering Fracture*

Mechanics 168 (décembre 2016): 93 104. <https://doi.org/10.1016/j.engfracmech.2016.02.045>.

- 435 [31] Fedele, R., B. Raka, F. Hild, et S. Roux. « Identification of Adhesive Properties in GLARE Assemblies Using Digital Image Correlation ». *Journal of the Mechanics and Physics of Solids* 57, 7 (1 juillet 2009): 1003 16. <https://doi.org/10.1016/j.jmps.2009.04.005>.
- [32] Vargas, R, J. Negggers, R B Canto, J A Rodrigues, et François Hild. « Comparison of two full-field identification methods for the wedge splitting test on a refractory ». *Journal of the European Ceramic Society* 38, 16 (2018): 440 5569 79. <https://doi.org/10.1016/j.jeurceramsoc.2018.07.039>.
- [33] Vargas, R, R B Canto, et François Hild. « On the Calibration of Cohesive Parameters for Refractories from Notch Opening Displacements in Wedge Splitting Tests ». *Journal of the European Ceramic Society* 41, 14 (2021): 7348 61. <https://doi.org/10.1016/j.jeurceramsoc.2021.07.011>.
- [34] Vargas, R., R. B. Canto, et F. Hild. « Fracture Energy Evaluation of Refractories in Wedge Splitting Tests from Notch Opening Displacements ». *Journal of the European Ceramic Society* 41, 10 (1 août 2021): 445 5367 79. <https://doi.org/10.1016/j.jeurceramsoc.2021.02.055>.
- [35] Doitrand, Aurelien, Ronan Henry, Hassan Saad, Sylvain Deville, et Sylvain Meille. « Determination of interface fracture properties by micro- and macro-scale experiments in nacre-like alumina ». *Journal of the Mechanics and Physics of Solids* 145 (2020): 104143. <https://doi.org/10.1016/j.jmps.2020.104143>.